Low cost Hyper-spectral imaging system using Linear Variable Bandpass Filter for Agriculture Applications

SHIGENG SONG[1], DES GIBSON[1*], SAM AHMADZADEH[1], HIN ON CHU[1], BARRY WARDEN[2], RUSSELL OVEREND[2], FRASER MACFARLANE[3], PAUL MURRAY[3], STEPHEN MARSHALL[3], MATT AITKENHEAD[4], DAMIAN BIENKOWSKI[5], RUSSELL ALLISON[6]

[1,] Institute of Thin Films, Sensors & Imaging, SUPA, University of the West of Scotland, Scotland PA1 2BE;

[2,] Wideblue Ltd, Glasgow;

[3,] Dept. Electronic and Electrical Engineering, University of Strathclyde, Royal College Building, 204 George Street, Glasgow;

[4,] The James Hutton Institute, Aberdeen AB15 8QH, Scotland, UK;

[5,] The James Hutton Institute, Dundee DD2 5DA, Scotland, UK;

[6,] Galloway & MacLeod Ltd. South Lanarkshire, UK

*Corresponding author: des.gibson@uws.ac.uk

Abstract: Hyperspectral imaging for agricultural applications provides a solution for non-destructive, large-area crop monitoring. However, current products are bulky and expensive due to complicated optics and electronics. A linear variable filter was developed for implementation into a prototype hyperspectral imaging camera that demonstrates good spectral performance between 450nm – 900nm. Equipped with a feature extraction and classification algorithm, that can be used to determine potato plant health with ~88% accuracy. This algorithm was also capable of species identification and is demonstrated as being capable of differentiating between rocket, lettuce and spinach. Results are promising for an entry-level, low-cost hyperspectral imaging solution for agriculture applications.

OCIS Codes: (310.1860) Deposition and fabrication; (310.6845) Thin film devices and applications; (110.4234) Multispectral and hyperspectral imaging.

1. Introduction

Crop monitoring has been of significant importance in recent years, particularly for improved crop yield and food security. The ability to know which areas in a field require attention, can prevent localized drought and spreading of disease. This is difficult to do manually considering the scale of the task, new technologies such as LiDAR, multispectral and hyperspectral imaging (HSI) solutions have addressed these challenges. HSI has great potential in agriculture applications, particularly for disease detection [1-4], plant development [5] and large area soil nutrient content monitoring [6]. These technologies also reduce the training and experience required to perform the same task manually. For example, basal stem rot (BSR) is a fatal fungal disease of palm oil plantations and Liaghat et al. (2014) [1] used reflectance spectroscopy analysis, in the visible to near infrared region (325-1075 nm) to assess this disease. This analysis determined whether the health of palm leaf samples were from healthy, slightly damaged, moderately damaged and heavily damaged trees. Their results achieved rapid screening of BSR in palm using spectral analysis. Sankaran

et al. (2013) [4] demonstrated use of visible-near infrared and mid-infrared spectroscopy to distinguish whether citrus leaves were infected with canker, with a classification accuracy of ~90%. Liu et al. (2014) [5] monitored, non-destructively, changes of chlorophyll content for field plants, using a real-time monitoring system based on visible and near-infrared reflection spectroscopy. Their investigation validated adequate performance of spectral analysis by comparing the results with chlorophyll index determined by the standard instrumentation. Their investigations also indicated that reflectance at 700 nm is a sensitive indicator of chlorophyll concentration. Linear variable filters (LVFs) provide an alternative optical system to diffraction gratings, as seen in a study by Emadi [7] et al. (2012) who developed a Fabry-Perot type LVF for an ultraviolet micro-spectrometer; for potential applications in atmospheric gas sensing and pharmaceutical analysis. Citing an advantage from LVFs not requiring moving parts which is particularly important for effective space utilization. However, due to its optical assembly the spectrometer was rather bulky and has low sensitivity in the UV region. An issue with producing LVFs is that they are relatively complicated optical filter designs, so volume production is an issue, however, L. Abel-Tiberini [8] specifically

1

developed masking mechanisms to produce LVFs with high throughput. This process has difficulties achieving desired thickness gradients for variable filters. While the potential of these spectral analysis systems seem promising, current HSI systems are bulky and expensive. This makes it difficult to expand their usage, with pricing of these systems typically on the order of $10,000s. This article addresses these issues, designing a low cost, portable HSI camera for agritech by utilizing novel linear variable bandpass filters (LVFs). The Hyperspectral Crop Camera (HCC), was developed and prototyped. These LVFs significantly reduce spectrometer size and cost.

2. LVF Fabrication

A. Equipment and Process

Deposition of the Linear Variable Filter (LVF) was carried out using a microwave plasma assisted pulsed DC reactive sputtering process. Mechanical masking to achieve spatial variation in bandpass centre wavelength across the substrate surface was applied. Figure 1, shows the configuration of the deposition system. This employs a horizontally mounted rotating drum, where substrates are mounted, with configurable flanges for target masks. A microwave-plasma source is set up at the top of the system.
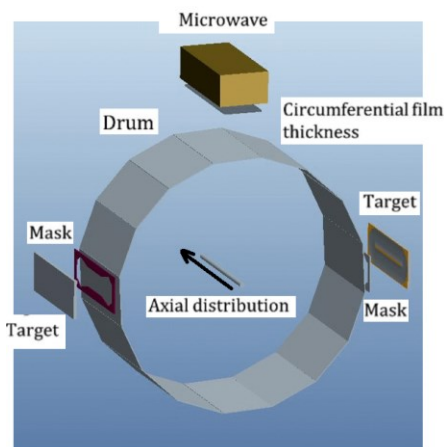

Figure 1. Schematic of Microwave Assisted Pulsed DC rotating drum Sputter deposition System with mechanical masking, used to deposit novel LVFs. This shows targets, masks, the microwave, circumferential direction, and axial distribution direction.

The drum rotation speed is such that two monolayers are deposited per pass across the magnetron targets, thereby allowing full oxidation of the metal rich sputtered film in the separate microwave plasma region. One key advantage of the microwave plasma in this pulsed-DC reactive sputtering system is its separated sputtering and oxidation zones. Only argon gas is introduced at the target region and oxygen in the microwave plasma zone. This provides metal-like sputtering and separated microwave plasma assisted oxidation enables high deposition rates and high-quality films with less pin holes to be achieved.

The critical deposition rate for this process has been investigated previously with the use of an adjustable mask placed between targets and rotating drum, in order to produce the desired LVFs. A significant advantage of a drum produced LVF is the avoidance of curvature for the same wavelength line.

Figure 2 shows an example of an LVF produced with this deposition system with XY axes. This drum-based system has great uniformity along the circumference of the drum, thus producing a linear thickness gradient along x-axis and uniform thickness along transverse direction (y-axis) [9].

Figure 2. Exemplar LVF orientation with y-axis representing the linear uniformity and x-axis representing the linear thickness gradient.

To improve the coatings several measures were taken:
- Pulsed DC sputtering is employed to suppress arcing
- Non-microwave assisted plasma produces molecular oxygen whereas with the addition of microwave atomic oxygen can be achieved. As a result oxygen is more readily available to react with each layer passing by for a more uniform oxidation of the coating therefore, resulting in much improved film homogeneity
- The Deposition of a metal layer first reduces the chance of pin-hole formation allowing for higher optical densities films.
- Utilizing a partial pressure controller permits for total control of oxygen partial pressure. In turn uniform oxidization of the film can be achieved as oxygen reactivity varies thorough the process.

Dielectric materials used to produce the optical filter are Niobium and Silicon (purchased from Testbourne Ltd. - 99.99% Pure - and were used as received) for high/low refractive index, Nb_2O_5 and SiO_2 respectively [10]. In order to produce a film with varying thicknesses across the surface, a custom uniformity mask had to be utilized. To produce such a mask for an optical filter as complicated as these LVFs, mask design is taken into great consideration.

B. Mask Design for Linear Gradient Thickness

A programme was written to design deposition masks that produces the desired thickness distributions for a configuration of substrates on a rotating drum, a target, and a mask with pre-defined shape function [11]. As depicted in Figure 3. In order to optimize the mask to achieve desired thickness distribution, several variables are considered; the sputtering yield, angular distribution of the ejected particles of the target, the mask restriction function, the arriving angle of sputtered particles on the substrate, as well as the substrate movement.
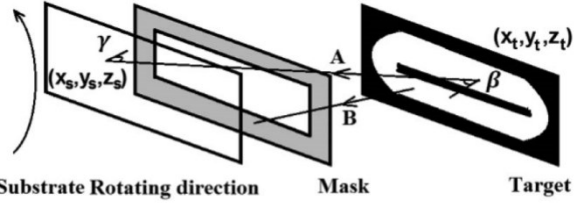
Figure 3. Schematic of the sputtering geometry, where the substrate is mounted on a rotating drum, β is the ejected particle flux emission angle to the target surface normal, and γ is the deposited particle flux incident angle to the substrate surface normal. On path A, the particle reaches the substrate, and on path B, the particle is blocked by the mask. This is generated directly from the measurement of the target erosion track profile.

The magnetic field was calculated and fed into the semi-empirical model to create the etch profile of the dielectric materials (targets). The Etch profile is calculated by taking into account the integration of ion energy along approximate ion path. By relating the magnetic field, $B_{tan,}$ to the erosion track profile, a 2D data array is obtained as *trackyeild*. Ejected atoms angular distribution is a function of the angle of incidence of the incident bombardment beam. Using pulsed-DC magnetron sputtering this angle is almost at the normal to the target surface. Considering turbulent electric field collisions, a Monte Carlo simulation determined a mean incident angle close to normal incidence for this simulation.

Angular distribution can be reduced to two unknowns, described as:

$$f(\beta) = \cos(\beta - \beta_0)^n \qquad (1)$$

Where, $f(\beta)$ is the angular distribution function of ejected atoms and β_0 is the angle of maximum emission.

For each point source, particle arrival rate is proportional to the inverse square of the distance between target and substrate. $\cos(\gamma)$ corrects for the drum and substrate rotation (γ being the angle between the beam/substrate and normal incidence). A further function *passrate* determines whether the mask blocks material arriving to the substrate.

$$probability = \frac{\cos(\beta-\beta_0)^n \times Trackfield \times passrate \times \cos(\gamma)}{r^2} \qquad (2)$$

The target and substrate coordinates, (X_t, Y_t, Z_t) and (X_s, Y_s, Z_s) respectively, are meshed with sum probabilities of all target elements determining relative thickness. Film thickness is circumferentially uniform, therefore only two substrate coordinates are required to be derived. A specific dataset is determined using coordinates $X_s, Y_{s0} - Rsin(\theta), Z_{s0} - Rcos(\theta)$ for the point X_s at the centerline and moved to the θ angle, shown in figure 3. Here, (X_s, Y_{s0}, Z_{s0}) are the coordinates on the rotating axis. The final relative thickness at point Xs can be obtained by integrating θ for a range of $(-\theta_0, \theta_0)$. The final equation for thickness simulation is:

$$Thickness\ (X_s) = \sum_\theta \sum_{X_t, Y_t, Z_t} \frac{\cos(\beta-\beta_0)^n \times Trackfield \times \cos(\gamma)}{r^2} \qquad (3)$$

Thus, using these functions with a desired thickness distribution for the LVFs, a mask geometry was designed. This was then used in the microwave plasma assisted pulsed-DC reactive sputter deposition configuration to yield high quality LVFs.

C. Deposited LVF

LVFs, as seen in Figure 4, were produced as a result of optimised target mask design. This calculated shape matches the thickness distribution required to the gradient structure of the deposited LVF, shown in figure 5.

Figure 4. Thickness distribution of thin film layer on substrate produced using masks determined by simulation for accurate gradient structure.

Masked depositions have resulted in LVFs with observable distinctions between colors, as this is affected by the thickness distribution. Figure 5, shows an Photograph of two LVFs produced by the above mentioned optimised process, these allow linear spectral transmission /reflection tuning along the x axis of the filter, while the optical properties remain uniform along the filter's y axis.
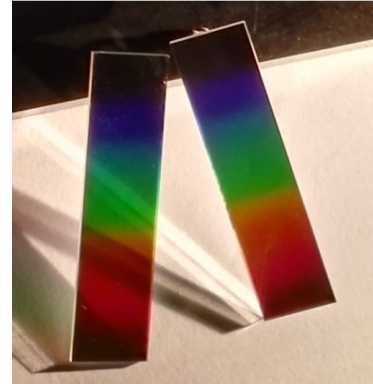

Fig 5. Example of fabricated LVF with distinctive color gradient representing linear thickness gradient.

Spatially linear variable visible bandpass filters were produced that allowed for high optical performance from 450 nm to 900 nm. Figure 6, show the optical transmission and peak transmission wavelengths as a function of position on the LVFs.
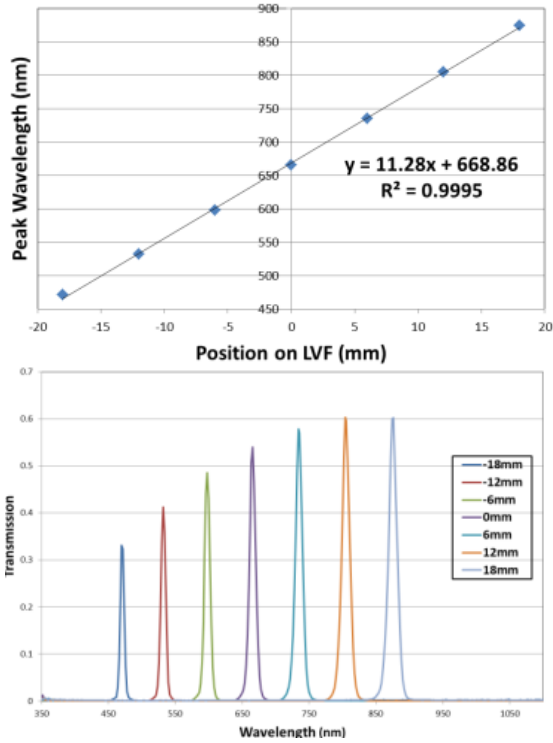
Figure 6. Linearity and passbands of 450 to 900 nm LVF.

These wavelengths enable studies with multispectral and hyperspectral imaging techniques, in particular with applications in agriculture.

3. Camera Development
A. hardware structure and constituents

The HCC design requires LVF position manipulation. A step motor with custom designed rack and pinion allowed translation of a Linear Variable Filter (LVF) across a standard high spatial resolution monochromatic image sensor (1.3MP IDS E2V CMOS Image Sensor). This creates discrete vertical strips at linearly spaced wavelengths in each image. Figure 7 shows a basic schematic of the imaging aspects of the HCC.
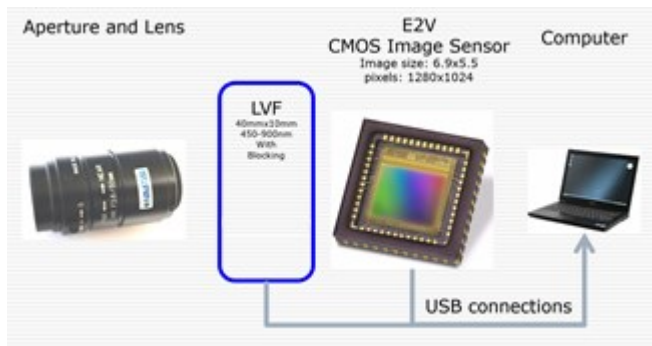

Figure 7. Basic components and LVF in camera set up.

To translate the LVF, it was bonded to a custom 3D printed holder. The holder was linked to a high-resolution step motor via a rack and pinion arrangement. The Ratio of the gearing was selected as to maximize the resolution of linear movement, where one step from the motor equated to 0.1mm

linear movement. Using this design the LVF can be precisely translated at relatively high speed. Capable of covering the full length for a full high resolution spectral scan, with adjustable exposure times for different lighting conditions. The HSI camera is also capable of multi-spectral and lower-spectral resolution imaging that can be achieved in less time. LVF position was controlled with an infrared optical sensor and the LVF returned to a known *home position* before each image scan. Positioning of the LVF was found to be both accurate, consistent and repeatable.

B. Wavelength Calibration

Once fully assembled, the prototype HCC was calibrated, using Hydrogen and Helium gas discharge lamps. Discrete wavelengths of these gas discharge lamps were used to correlate step position to wavelength for the LVF. H and He were chosen as both have several distinct emission lines in the visible spectrum. The lamps were imaged using a high resolution scan over the entire LVF spectral range from 450nm to 900nm. The expected step position was compared to the actual step position that each of the discharge lines that appeared in the calibration images. An adjustment was then made to the starting position of the scan to bring the theoretical step position of the wavelength in line with the actual step position. Once calibrated the device was then compared to the wavelength data from the LVF. The measured LVF data was then used to create a linear plot of wavelength vs step position, see Figure 8 and table 1. This plot was used to calibrate the LVF step position, corresponding the H and He gas lamp discharge peaks with corresponding step positions. Once calibrated the H and He emission lines correspond very well with the expected step position with the error between expected wavelength and the actual wavelength measured by the HCC found to be no greater than ±5nm.
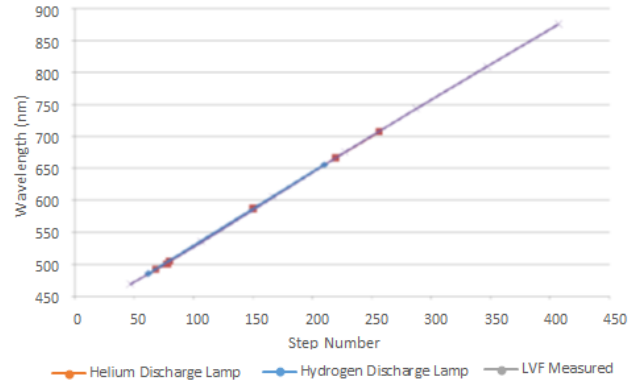

Figure 8. Shows the successful calibration of LVF step positions and correlating wavelengths (linear relation).

Table 1: LVF step position, corresponding the H and He gas lamp discharge peaks with corresponding step positions.

Actual wavelength λa (nm)	Emission Line Detected at step	Step Position Converted to Wavelength λb (nm)
486	64	488
492	70	495

501	78	506
505	80	508
587	152	586
656	210	653
667	224	665
707	260	705

Testing the proof of principle system showed good results confirming that the manipulation of the LVF position was both accurate and repeatable.

C. Performance of the HCC

The HCC was developed as a low cost hyperspectral imaging camera and as part of the development of the device, the HCC was benchmarked against a high end pushbroom hyperspectral system. For reference, the HCC device was approximately 1/10th of the cost of the pushbroom benchmark device.
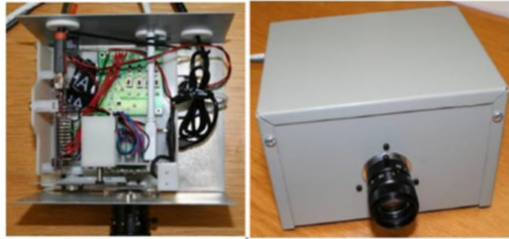

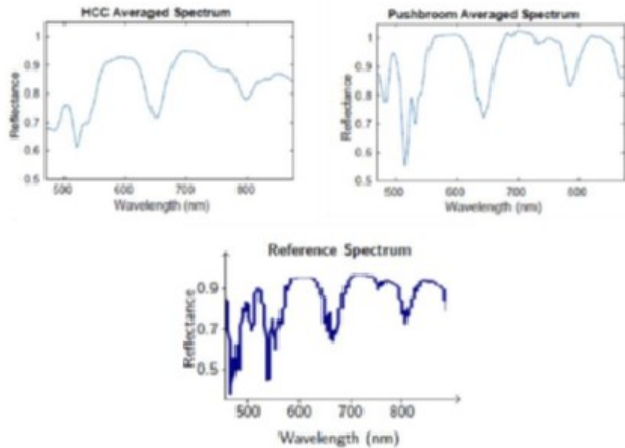Figure 9. Prototype HCC assembly with internals exposed and as a final compact design.

Figure 10. A Lab sphere certified reflectance standard (left) was used to characterize the HCC (middle) and pushbroom (right) system and compared against the reference spectrum

Spectra acquired by the HCC and the traditional pushbroom HSI system are highly correlated, as seen in Figure 10, both closely resemble the manufacturer's reference spectrum in between 450nm – 900nm. The spatial and spectral resolution of both systems with comparable parameter settings were compared with results shown in figure 11.

Table 2: Spectral and spatial resolution for prototype and traditional pushbroom HSI system, with similar settings.

	Spectral Resolution	Spatial Resolution
HCC	4.53nm	1280 x 1024
Pushbroom	2.44nm	377 x 336

While the spatial resolution of the HCC is far superior to that of the pushbroom system, the spectral resolution of the pushbroom system is approximately twice that of HCC when comparable settings. In spite of the reduced spectral resolution, as would be expected due to the device being in the prototype stage; the spectral data acquired by the HCC is accurate when compared to the reference reflectance standard and has been demonstrated to allow for accurate data acquisition.

4. Data Analysis and Classification of Plant Life

A. Data Capture and Reordering

The prototype HCC camera captures images in 3-dimensional hyperspectral data-cubes by translating the LVF across the field of view, capturing a set of images with discrete vertical strips at linearly spaced wavelengths over subsequent steps in time. As a result, the spatial and spectral information is spread over multiple successive images. This method of capturing hyperspectral data is known as spatio-spectral imaging and an example is shown visually in Figure 12.
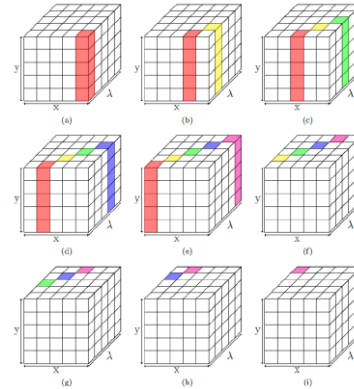

Figure 11. Temporal steps in capturing a hyperspectral image using the spatio-spectral method

A reordering algorithm was developed in order to manage camera data segments into wavelength dependent images for analysis. This is done in order to obtain a more traditional representation of a hyperspectral datacube, where each wavelength is contained in one plane and each successive frame represents an increasing wavelength. With this reordering algorithm, the data captured using the HCC is equivalent to that captured using a traditional pushbroom sensor.

In order to validate the HCC's usefulness in crop monitoring and classification, two distinct datasets were acquired. The first consisted of images containing three types of salad leaves and was intended to determine whether images captured using the HCC would be sufficient in differentiating these species. The second dataset consisted of select leaves collected from potato trial fields at JHI, where select plants had been exposed to late blight, a common disease in potato crops.

These datasets were then employed in support vector machine (SVM) classification for these two tasks, where a multiclass SVM was used to determine the species of leaf in the first task and a binary SVM to differentiate between healthy and unhealthy areas on the leaves in the second task.

B. Feature Extraction and Dimensionality Reduction

Regions of interest (ROIs) have to be extracted from the image by visual inspection. After ROIs have been determined, the relevant spectra were extracted and class labels assigned. *Standard Normal Variate* (SNV) is a common tool in Hyperspectral data pre-processing [12, 13]. This was applied to correct for noise and scatter effects. spectrum in the hyperspectral datacube, $x_{i,j}$, is normalised by subtracting its mean value, $\overline{x_{i,j}}$, before being divided by the standard deviation, $\sigma_{x_{i,j}}$, of the spectra :

$$x_i(SNV) = \frac{x_i - \overline{x_i}}{\sigma_{x_i}} \qquad (4)$$

This process creates a set of spectra where the average of each spectrum is zero with variance of one
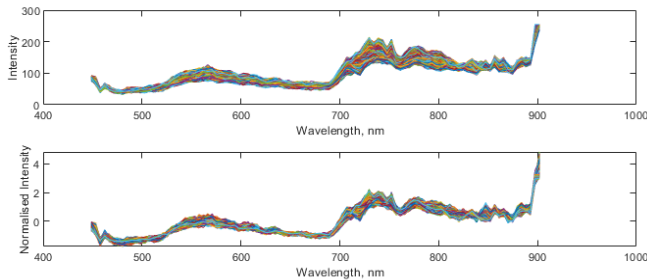

Figure 12. Effect of SNV on a set of spectra, normalised spectrum with reduced noise and interference.

Employing SNV normalisation results in the negation of disparity caused by changes in illumination or noise scattering through the removal of the mean bias. With a normalised intensity, like-pixels with similar spectra should be classified similarly despite the differences in original illumination. PCA, also known as the discrete Karhunen–Loève Transform or the Hotelling Transform [14], can be used as both feature extraction and dimensionality reduction, making it a common statistical technique used in HSI analysis [15]. PCA attempts to capture the most variance within a data set whilst reducing the number of components needed to recreate the original dataset. Representing a highly correlated high dimensional dataset in a lower dimensional space. This is significantly less computationally intensive and in turn quickens processing analysis and classification [16]. PCA computes the covariance matrix from the SNV normalised data cube. Eigenvalues and Eigenvectors can be extracted from this covariance matrix by Eigen decomposition. By reordering the Eigenvalues in a highest to lowest list, can be used to recreate a representation original dataset, while discarding redundant information, in a new subspace.

C. Support Vector Machines Testing - Data Prediction and Classification

The dimensionally reduced dataset has to be test/train split with random sampling. A subset (typically lower than 10%) of all spectra is selected to form a training set for a classifier, whilst the remaining data is used for testing and accuracy of a trained SVM [17]. For HSI datasets SVMs are a common classification technique [18]. SVMs attempt to classify data into distinct groups by virtually drawing a maximum margin hyperplane between groups or clusters of data points. Often the data is not linear and has to be separated using a kernel trick [19]. This shifts data into a higher dimension and splits a hyperplane between data clusters in a z-direction as opposed to standard x-y plane. SVM is a binary technique however, adopting a one vs all method allows for multiple groupings/clusters to be classified. SVM models have to be trained, by exposing the model to examples of groupings/classes the model attempts to find an ideal solution by iteration. Using a trained model the SVM can predict and classify never before seen data into the classes selected during training. The algorithm for data analysis and classification of crop types and crop diseases was developed.

D. Classification of Salad Leaves

The ROIs were extracted to distinguish between three types of salad leaves, namely spinach, rocket and lettuce and split into a test set and a training set. Using the training set to make prediction equations for an SVM classifier. The accuracy was evaluated on the test set. PCA was used for dimensionality reduction and feature extraction. The SVM used the Radial Basis Function (RBF) Kernel and selected the optimal parameters grid search using k-fold cross-validation. The results of the SVM classifier in figure 14 and accuracies in Table 3.
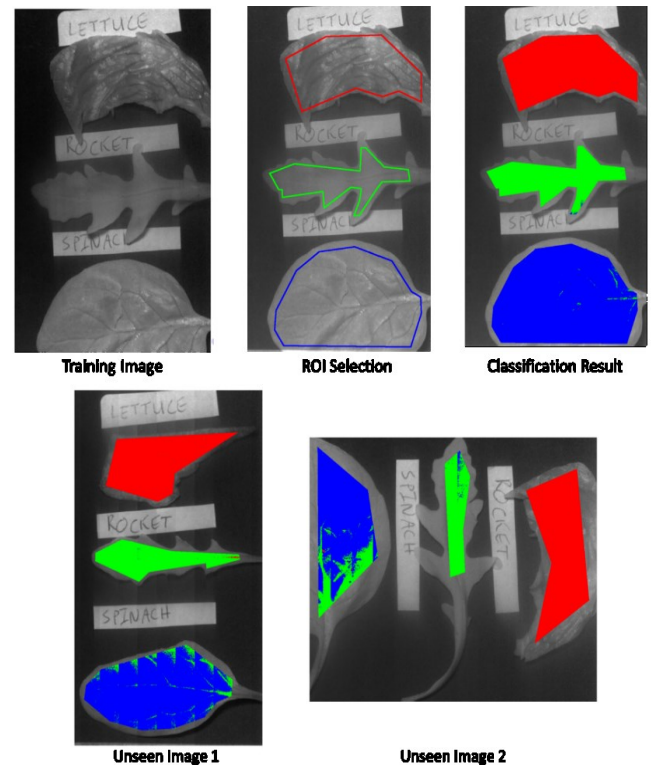

Figure 13. Classification of salad leaves with accuracy using the decision/classification algorithm. Demonstrating the camera distinguishing differences in similar leaf types.

Table 3: Results of the SVM classifier on unseen images.

Class	Training Image	Unseen Image 1	Unseen Image 2
Lettuce	99.99%	99.97%	100.00%
Rocket	99.64%	99.43%	96.54%
Spinach	99.27%	92.59%	78.12%

Aside for some visible confusion between spinach and rocket the SVM classifies the individual types of salad leaves very effectively. This implies that the clusters of data are separable and that the SVM-based model is highly accurate.

E. Classification of healthy and unhealthy potato crops

To classify late blight in potato crop, both healthy and diseased leaves were collected and mounted on a black card background for imaging. The data provided from HSI imaging was subject to the same procedure of analysis, both pre and post processing. Using a subset of the data as training and testing data by random sampling. An SVM was trained and applied for classification of spectra from healthy and diseased leaves. Once trained, the model was applied to classify the test data and the results of classifying two potato plots with "Orchestra" variety, plots 6 and 20 in the trial which contained both healthy leaves and some displaying symptoms of blight.. The healthy and unhealthy leaves were used to train an SVM to distinguish between areas displaying the symptoms of late blight versus healthy areas and this was tested using leaves which . The results from plot 6 are shown in Figure 15, where the leaves in the top left image are healthy and the leaves in the top right image are diseased. For training data 10% of pixels in two leaves from each set were used to train our SVM to recognise the spectra of healthy/unhealthy leaves before using it to classify each of the leaves.
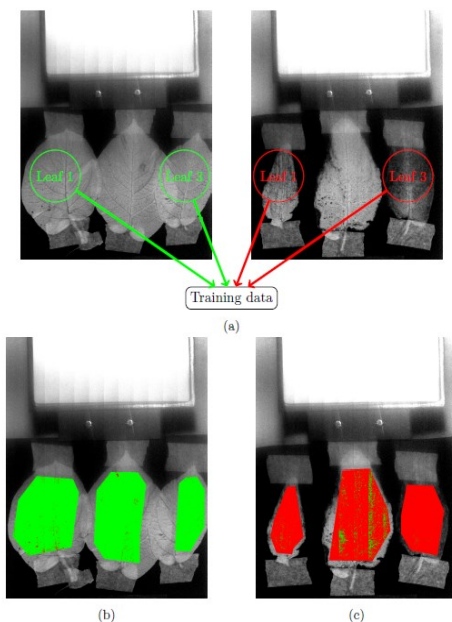

Figure 14. Supervised classification of the HCC image of plot 6 "Orchestra" using a trained SVM

The leaves are mostly classified correctly, if a majority voting approach was used each would be classified entirely as healthy or unhealthy based on the dominant class. In the previous examples, the majority of each leaf was showing healthy or unhealthy characteristics. In the leaves taken from plot 20, another "Orchestra" variety, small regions were displaying signs of blight. One such region was selected as the unhealthy training data and a balanced number of pixels was selected to be the healthy training data. Again, these samples were used to train a model using an SVM which was used to classify the rest of the testing pixels. The results of this classification are shown in Figure 16.
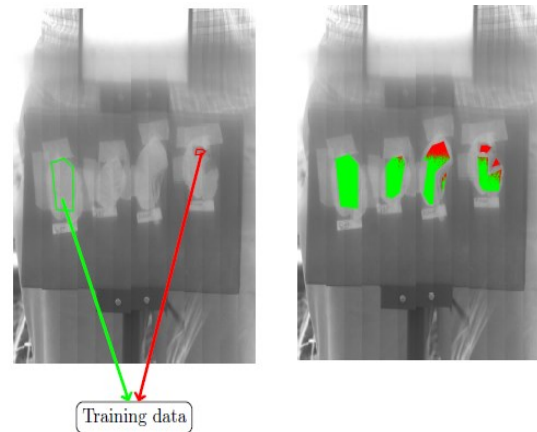

Figure 15. Supervised classification of the HCC image of plot 20 "Orchestra" using a trained SVM

This resulted in 88% accuracy in discriminating between healthy and unhealthy pixels. Given that several of the infected plants imaged were not symptomatic at the time of imaging, this level of accuracy is promising. It indicates that the HCC can be used to detect crop pathogen infection at an early stage, enabling time for treatment and avoidance crop yield loss.

5. Conclusion

A cost effective visible to near-infrared LVF was developed, using our custom deposition mask design. This enabled volume production of LVFs with controlled thickness distributions. These LVFs in conjunction with a suitable detector system can reduce costs, weight and size. A low-cost HSI camera was manufactured using the developed LVFs, with performance comparable with commercial alternatives. This provides a high price-to-performance value proposition. Compared to a high end pushbroom hyperspectral imaging system with similar specifications, the HSI prototype camera was comparable while only costing approximately 10% of the reference system. An algorithm for the HCC system shows good feature extraction and SVM classification between similar leaf varieties and achieved ~88% accuracy in discriminating healthy and late blight expressing classes of potato plant leaves. These results are promising for future applications of the low-cost HSI camera, including potential for aerial and satellite monitoring.

6. References

1. S. Liaghat et al. "Early detection of basal stem rot disease (Ganoderma) in oil palms based on hyperspectral reflectance data using pattern recognition algorithms", International Journal of Remote Sensing 35(10):3427–3439 (2014)

2. G. Giovanelli et al. "NIR spectroscopy for the optimization of postharvest apple management", Postharvest Biology and Technology, 87. 13–20. 10.1016 (2014)

3. M.A. Shahin, S Symonsand D Hatcher, "Quantification of Mildew Damage in Soft Red Winter Wheat Based on Spectral Characteristics of Bulk Samples: A Comparison of Visible-Near-Infrared Imaging and Near-Infrared Spectroscopy", Food and Bioprocess Technology, 7. 10.1007/s11947-012-1046-8 (2014)

4. J. R. Davis, Heat-resistant materials, ASM International, 1997S. Sankaran, L Khot and R Ehsani, "Mid- and Far-infrared Imaging" in book "Imaging with Electromagnetic Spectrum: Applications in Food and Agriculture" 129-146. 10.1007/978-3-642-54888-8_7 (2014)

5. B Liu, et al. "Plant leaf chlorophyll content retrieval based on a field imaging spectroscopy system" Sensors (Basel, Switzerland) vol. 14,10 19910-25 (2014)

6. R Vašát et al "Consideration of Peak Parameters Derived from Continuum-Removed Spectra to Predict Extractable Nutrients in Soils with Visible and Near-Infrared Diffuse Reflectance Spectroscopy (VNIR-DRS)", Geoderma, 232–234. 208 - 218. 10.1016 (2014)

7. A. Emadi, et al, "Linear Variable Optical Filter-based Ultraviolet Microspectrometer", Applied Optics, 51,19(2012)4308-4315

8. L. Abel-Tiberini, F.Lemarquis and M.Lequime, "Masking Mechanisms Applied to Thin Film Caotings for the Manufacturing of Linear Variable Filters for Two-dimensional Array Dectrors", Applied Optics 47,30(2008)5706-5714

9. S. Song, F. Placido, Applied Physics Letters, 99(2011)121901].

10. S Song, C Li, H Chu, D Gibson, "Reactive Dynamics Analysis of Critical Nb2O5 Sputtering Rate for Drum Based Metal-like Deposition", Applied Optics, , 56, 4(2017)206

11. C Li, S Song, D Gibson, D Child, H Chu, E Waddell, "Modeling and validation of uniform large-area optical coating deposition on a rotating drum using microwave plasma

12. R. J. Barnes, M. S. Dhanoa, & S. J. Lister. Standard normal variate transformation and de-trending of near-infrared diffuse reflectance spectra. Applied spectroscopy, 43(5), 772-777. (1989)

13. Å Rinnan, F. Van Den Berg, & S. B. Engelsen,. Review of the most common pre-processing techniques for near-infrared spectra. TrAC Trends in Analytical Chemistry, 28(10), 1201-1222. (2009)

14. H. Abdi, & L. J. Williams,. Principal component analysis. Wiley interdisciplinary reviews: computational statistics, 2(4), 433-459. (2010)

15. J. Ren, J. Zabalza, et al., "Effective feature extraction and data reduction with hyperspectral imaging in remote sensing," IEEE Signal Processing Magazine, (2014).

16. J. Zabalza, J. Ren, et al., "Novel folded-pca for improved feature extraction and data reduction with hyperspectral imaging and sar in remote sensing," ISPRS Journal of Photogrammetry and Remote Sensing].

17. T. Rumpf, A. K. Mahlein, U. Steiner, E. C. Oerke, H. W. Dehne, & L Plümer. Early detection and classification of plant diseases with support vector machines based on hyperspectral reflectance. Computers and electronics in agriculture, 74(1), 91-99. (2010)

18. F. Melgani and L. Bruzzone, "Classification of hyperspectral remote sensing images with support vector machines," IEEE Transactions on Geoscience and Remote Sensing, (2004)

19. T. Hofmann, B. Schlkopf, et al., "Kernel methods in machine learning," Ann. Statist., (2008)